

Dynamic Modes of Microcapsules in Steady Shear Flow: Effects of Bending and Shear Elasticities

Hiroshi Noguchi*

Institute for Solid State Physics, University of Tokyo, Kashiwa, Chiba 277-8581, Japan

(Dated: November 14, 2018)

The dynamics of microcapsules in steady shear flow was studied using a theoretical approach based on three variables: The Taylor deformation parameter α_D , the inclination angle θ , and the phase angle ϕ of the membrane rotation. It is found that the dynamic phase diagram shows a remarkable change with an increase in the ratio of the membrane shear and bending elasticities. A fluid vesicle (no shear elasticity) exhibits three dynamic modes: (i) Tank-treading (TT) at low viscosity η_{in} of internal fluid (α_D and θ relaxes to constant values), (ii) Tumbling (TB) at high η_{in} (θ rotates), and (iii) Swinging (SW) at middle η_{in} and high shear rate $\dot{\gamma}$ (θ oscillates). All of three modes are accompanied by a membrane (ϕ) rotation. For microcapsules with low shear elasticity, the TB phase with no ϕ rotation and the coexistence phase of SW and TB motions are induced by the energy barrier of ϕ rotation. Synchronization of ϕ rotation with TB rotation or SW oscillation occurs with integer ratios of rotational frequencies. At high shear elasticity, where a saddle point in the energy potential disappears, intermediate phases vanish, and either ϕ or θ rotation occurs. This phase behavior agrees with recent simulation results of microcapsules with low bending elasticity.

PACS numbers: 87.16.D-, 05.45.-a, 82.40.Bj

I. INTRODUCTION

Soft deformable objects such as liquid droplets [1, 2], lipid vesicles [3–24], red blood cells (RBCs) [25–41], and synthetic capsules [42–51] exhibit rich behaviors in flows. In recent years, they have received growing attention experimentally, theoretically, and numerically. These objects are filled with liquids and have a constant internal volume V . The lipid vesicles, RBCs, and synthetic capsules are wrapped by lipid or polymer membranes and resist breaking up under much larger shear than liquid droplets. The variation of material properties of these objects can lead to different dynamic modes with morphological changes.

Since microcapsules can carry substances and control their release, they are widely used in various fields including food, printing inks, pharmaceuticals (drug carrier for drug delivery system), agrochemicals, and cosmetics. Various kinds of microcapsules are synthesized with different sizes and membrane thicknesses h [42, 43, 52–54]. The deformability of microcapsules can be varied widely by controlling the membrane elastic properties and capsule shapes. When the membrane is made of linear-elastic material, two-dimensional Young's modulus $Y_{mb} \equiv 4\mu K_A/(\mu + K_A) = Yh$ and the bending modulus $\kappa = Yh^3/12(1-\nu^2)$, where μ and K_A are two-dimensional shear and area compression moduli, respectively, with three-dimensional Young's modulus Y and Poisson ratio ν [55]. Thus, thicker membranes become more difficult to bend than to stretch ($\kappa/Y_{mb} \propto h^2$).

RBCs have a composite membrane made of lipid membrane and attached spectrin network. The lipid mem-

brane is in a fluid phase and is almost incompressible. The spectrin network adds shear elasticity to the membrane. The bending and shear elasticities of RBCs are estimated by micropipette aspiration [26, 56] and optical tweezers experiments [57–59]: $\kappa \simeq 2 \times 10^{-19} \text{J}$ and $\mu \simeq 6 \times 10^{-6} \text{N/m}$.

The relative importance of bending and shear elasticities is determined by the dimensionless Föppl-von Kármán number $\gamma = Y_{mb}R_0^2/\kappa$, where R_0 is the mean radius of capsules or cells [60]. The buckling transition of capsules from spherical to icosahedral shape occurs at $\gamma_b \simeq 150$ [60]. Capsules with a linear elastic membrane have large values of $\gamma \gtrsim 100$ because $\gamma = 12(1-\nu^2)(R_0/h)^2$. Capsules with a composite membrane can also have small γ . In this paper, we investigate microcapsules with wide ranges of γ .

Recently, the dynamics of lipid vesicles in steady shear flow was intensively investigated [3–22]. A lipid vesicle can be considered as a microcapsule in the small limit of the shear modulus $\mu \rightarrow 0$. An isolated fluid vesicle exhibits three types of dynamic modes in a steady shear flow, with flow velocity $\mathbf{v} = \dot{\gamma}y\mathbf{e}_x$, where \mathbf{e}_x is a unit vector in the flow direction. When the viscosity of internal fluid η_{in} and membrane viscosity η_{mb} are low, the membrane exhibit a tank-treading (TT) rotation with a stationary shape and a constant inclination angle $\theta > 0$ [see Fig. 1(b)]. At high η_{in} or η_{mb} , the vesicle exhibit a tumbling (TB) motion, where θ rotates [see Fig. 1(c)]. Around the TT-TB transition viscosity with high shear rate $\dot{\gamma}$, a swinging (SW) motion appears [7–9, 13, 15–17, 21], where θ and the vesicle shape oscillate [see Fig. 1(d)]. This motion is also called trembling [7–9, 16, 17] or vacillating-breathing [13, 15]. These three types of motion can be understood by the perturbation theories for quasi-spherical vesicles [15–17] or a generalized Keller-Skalak (KS) theory for deformable ellipsoidal

*noguchi@issp.u-tokyo.ac.jp

vesicles [21].

Experimentally, synthetic capsules and RBCs show the oscillation (swinging) of their lengths and θ [28, 42, 43] during TT motion and RBCs also transit from TB to TT with increasing $\dot{\gamma}$ [28, 61]. Recently, this dynamics was explained by the KS theory with the addition of an energy barrier for the TT rotation caused by the membrane shear elasticity [28, 36]. More recently, we phenomenologically extended this theory [36] to include the shape deformation of RBCs [41]. Fix-shaped and deformable RBCs give very similar phase behavior. At low $\dot{\gamma}$, RBCs show TB (θ) rotation without TT (ϕ) membrane rotation. In the middle ranges of shear rate $\dot{\gamma}$, synchronized phases of the θ and ϕ rotations with integer ratios of the rotation frequencies as well as intermittent rotations [36] appear [41]. The TT-TB transition was also obtained by recent simulations of microcapsules [44–46]. However, the above intermediate phase (synchronized or intermittent rotations) was not observed in their simulations. Kessler *et al.* contested that intermittent rotation is an artifact of the theoretical model [44, 47]. As we describe below, the disappearance of the intermediate phase is found to be caused by low bending elasticity in their simulations. In this paper, we systematically investigate the dynamics of microcapsules in steady shear flow, and show that their phase behaviors are qualitatively changed from the bending-elasticity dominant condition to the shear-elasticity dominant condition.

Note that some confusion is caused by the different definitions of a tumbling state. For fluid vesicles, tumbling typically means the rotation of inclination angle accompanied by the rotation of the phase angle ϕ . On the other hand, for RBCs and capsules, it typically means the θ rotation accompanied by the ϕ oscillation (not rotation). Thus, in the definition for fluid vesicles, synchronized or intermittent rotations of θ and ϕ are also called “tumbling”. In this paper, we call them “TB with no TT” and “TB with TT” to distinguish their ϕ modes.

The dynamics of microcapsules is described by several dimensionless quantities. Here, dimensionless quantities are denoted by a superscript $*$. The relative ratio of the volume V and surface area S is characterized by the reduced volume $V^* = 3V/(4\pi S)^{3/2} = (R_V/R_S)^3 = (1 + \Delta_S/4\pi)^{-3/2}$, where $R_V = (3V/4\pi)^{1/3}$, $R_S = (S/4\pi)^{1/2}$, and the excess area $\Delta_S = S/R_V^2 - 4\pi$. The relative viscosity of the inside fluid and membrane are $\eta_{in}^* = \eta_{in}/\eta_0$ and $\eta_{mb}^* = \eta_{mb}/\eta_0 R_S$, where η_0 is the viscosity of the outside fluid. The bending rigidity κ is used as an energy unit, and the shape relaxation time of the fluid vesicles with bending rigidity κ is given by $\tau = \eta_0 R_S^3/\kappa$ (for $\eta_{in}^* = 1$). This time is used to define a reduced shear rate $\dot{\gamma}^* = \dot{\gamma}\tau$. Since the Reynolds number is low, $Re < 1$ in typical experimental conditions, the effects of the inertia are neglected.

The theoretical models of fluid vesicles and microcapsules are explained in Sec. II. The results are described in Sec. III. First, the dynamics of fluid vesicles ($\mu = 0$) is briefly explained in Sec. III A, and then dynamics

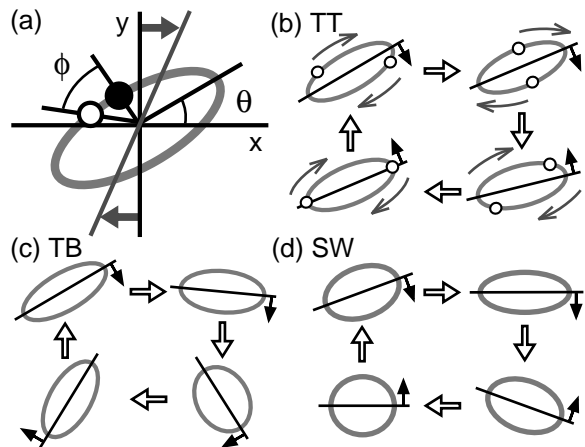


FIG. 1: Schematic representation of (a) a capsule and its dynamic modes: (b) Tank-treading (TT), (c) Tumbling (TB), and (d) Swinging (SW) modes. (a) The inclination angle θ and phase angle ϕ are depicted. The closed and open circles are the original and current positions of a membrane segment, respectively. (b) For an elastic capsule, a capsule shape and θ oscillate, while they are kept at fixed values for a fluid vesicle.

with low and high shear elasticity μ is described in Secs. III B–III D. The mechanism of the dynamic modes and experimental conditions are discussed in Sec. IV. The summary is given in Sec. V.

II. GENERALIZED KELLER-SKALAK THEORY

A. Fluid vesicle

Keller and Skalak [30] analytically derived the equation of motion of the inclination angle θ for vesicles or elastic capsules based on Jeffery’s theory [62]. The KS theory assumes (i) a fixed ellipsoidal shape of vesicles and (ii) a simple velocity field on the membrane. It gives very good predictions for vesicle dynamics at low shear rates. The KS theory is phenomenologically extended to include the shape deformation of fluid vesicles on the basis of the perturbation theory [12, 13, 16, 17] of quasi-spherical vesicles in Ref. [21]. The shape deformation is represented by the Taylor deformation parameter $\alpha_D = (L_1 - L_2)/(L_1 + L_2)$, where L_1, L_2 are the principal lengths on the vorticity (xy) plane, and L_3 is in the vorticity (z) direction. The differential equations of α_D and θ are given by

$$\frac{d\alpha_D}{\dot{\gamma}dt} = \left\{ 1 - \left(\frac{\alpha_D}{\alpha_D^{\max}} \right)^2 \right\} \left\{ -\frac{A_0}{\dot{\gamma}^*} \frac{\partial F^*}{\partial \alpha_D} + A_1 \sin(2\theta) \right\}, \quad (1)$$

$$\frac{d\theta}{\dot{\gamma}dt} = \frac{1}{2} \left\{ -1 + f_0 f_1 \cos(2\theta) \right\} - \frac{f_0 d\phi}{\dot{\gamma}dt}, \quad (2)$$

$$\frac{d\phi}{\dot{\gamma}dt} = -\frac{\cos(2\theta)}{2f_1 \{ 1 + f_2(\eta_{in}^* - 1) + f_2 f_3 \eta_{mb}^* \}}, \quad (3)$$

where $A_0 = 45/8\pi(32 + 23\eta_{in}^* + 16\eta_{mb}^*)V^*$ and $A_1 = 30/(32 + 23\eta_{in}^* + 16\eta_{mb}^*)$ [21, 23]. The first and second

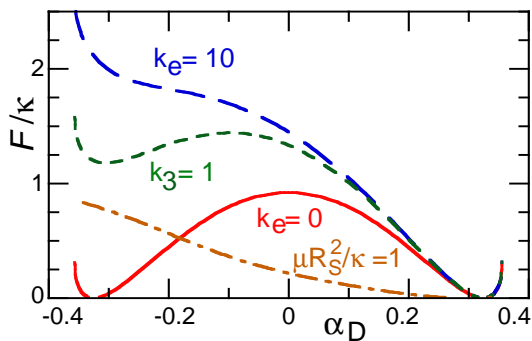


FIG. 2: Free-energy potential function of the Taylor deformation parameter α_D at $\phi = 0$ and $\phi = \pi/2$ [$F(-\alpha_D, 0) = F(\alpha_D, \pi/2)$]. Solid and long-dashed lines represent $k_e = 0$ and $k_e = 10$ with $k_3 = 0$, respectively. Short-dashed line represents $k_e = 10$ with $k_3 = 1$. Dashed-dotted line represents the potential of the shear elasticity estimated by the perturbation of quasi-spherical capsules with $\mu R_S^2/\kappa = 1$.

terms in the last parentheses of Eq. (1) represent the forces of the membrane bending elasticity and the external shear stress, respectively. The free energy is given by $F = F_{cv} \equiv (\kappa/2) \int (C_1 + C_2)^2 dS$, where C_1 and C_2 are the principal curvatures at each point of the membrane.

In Eq. (2), the factors f_0 , f_1 , f_2 , and f_3 are function of the vesicle shape (α_D , V^*) (see Appendix A). Because the factors and F are independent of the phase angle ϕ for fluid vesicles, Eq. (2) can be simply written as

$$\frac{d\theta}{\dot{\gamma} dt} = \frac{1}{2} \{-1 + B \cos(2\theta)\}. \quad (4)$$

The factor B is a function of α_D , V^* , η_{in}^* , and η_{mb}^* .

At $\eta_{in}^* = 1$, the lipid vesicle shows only the TT motion at any V^* and $\dot{\gamma}^*$. The TT steady angle θ_0 predicted by KS theory [Eq. (2)] gives very good agreement with simulations and experiments [4, 6, 11, 20, 23, 37]. On the other hand, the perturbation theories give TB motion even at $\eta_{in}^* = 1$ for $V^* \lesssim 0.8$, while they give good predictions for $V^* \gtrsim 0.9$ [23]. Thus, the perturbation theories should not be applied to the dynamics of vesicles and capsules for $V^* \lesssim 0.8$.

B. Microcapsule

Synthetic capsules and RBCs have membrane shear elasticity μ , which modifies their free-energy landscape: $F = F_{cv} + F_\mu$. The energy of the shear elasticity F_μ depends on the capsule shape and phase angle ϕ , while F_{cv} only depends on the capsule shape. The angle $\phi = 0$ is the original position in the absence of flow. During ϕ (TT) rotation, the membrane is locally elongated and it generates a free-energy barrier at $\phi = \pi/2$. Recently, Skotheim and Secomb extended the KS theory to take into account this free-energy barrier for capsules with

fixed ellipsoidal shapes [36]. Equation (3) is modified as

$$\frac{d\phi}{\dot{\gamma} dt} = -\frac{(c_0/\dot{\gamma}^*) \partial F^*/\partial \phi + \cos(2\theta)}{2f_1\{1 + f_2(\eta_{in}^* - 1) + f_2 f_3 \eta_{mb}^*\}}, \quad (5)$$

where $c_0 = 3f_2/8\pi f_1 V^*$ [36].

In this paper, we employ Eqs. (1), (2), and (5) to investigate the dynamics of the elastic capsule with prolate shape at $V^* = 0.9$ and $\eta_{mb}^* = 0$. These equations are numerically integrated using the fourth-order Runge-Kutta method. The curvature energy $F_{cv}(\alpha_D)$ is numerically calculated for the ellipsoidal vesicle. The prolate ($L_1 > L_2 = L_3$) and oblate ($L_1 = L_2 > L_3$ and $\alpha_D = 0$) shapes are energy minimum and maximum, respectively (see Fig. 2). Here, a fit function is employed to avoid the artifacts of nonsmooth functions: $\partial F_{cv}^*/\partial \alpha_D = 30\alpha_D - 820\alpha_D^5 - 1.7/\sqrt{\alpha_D^{\max} - \alpha_D} + 1.7/\sqrt{\alpha_D^{\max}}$ with $\alpha_D^{\max} = 0.356$. Here, the relative energy to the free-energy minimum (prolate shape) is considered. The force $-\partial F_{cv}/\partial \alpha_D$ diverges in the limit of maximum extension, $\alpha_D \rightarrow \alpha_D^{\max}(V^*)$. For shear elasticity, the leading-order energy function is employed in Secs. IIIB and IIIC: $F_\mu(\alpha_D, \phi)^* = (k_e/2)\{(\alpha_D - \alpha_0)^2 \cos^2(\phi) + (\alpha_D + \alpha_0)^2 \sin^2(\phi)\}$, where $\alpha_0 = 0.325$ is α_D of the prolate shape. Because compression and $\pi/2$ rotation can generate the same capsule state, the free energy should keep the relation $F(-\alpha_D, \phi) = F(\alpha_D, \phi + \pi/2)$. The shear elastic energy is estimated by the perturbation of quasi-spherical capsules; see Appendix B. The harmonic potential $F_\mu^*(\alpha_D, 0)$ with $k_e \simeq 4\mu R_S^2/\kappa$ gives good agreement with the perturbation result; see Fig. 2. In Sec. IIID, in order to check dependence on the potential shape, a higher-order term F_3 is added to the potential: $F_3^* = (k_e k_3/3)\{(\alpha_D - \alpha_0)^3 \cos^2(\phi) - (\alpha_D + \alpha_0)^3 \sin^2(\phi)\}$.

III. RESULTS

A. Fluid vesicle

First, we briefly describe the dynamics of lipid vesicles ($k_e = 0$) in steady shear flow. Figure 3(a) shows its phase diagram. At low viscosity ratio η_{in}^* , the vesicle shows a TT motion, where α_D and θ remain constant. The factor B in Eq.(4) is more than unity, and a stable fixed point $\theta = \theta_0 = 0.5 \arccos(1/B)$ and unstable fixed point $\theta = -\theta_0$ exist. As η_{in}^* increases, B and θ_0 decrease. At the critical viscosity $\eta_{in}^* = \eta_c^* = 5.27$, B becomes unity and the two fixed points $\theta = \pm\theta_0$ merge at $\theta = 0$ (saddle-node bifurcation). At $\eta_{in}^* > \eta_c^*$ with low shear rate $\dot{\gamma}^* \lesssim 1$, no fixed point exists so θ rotates (TB with TT); see Figs. 3(b-d). This TT-TB transition is quantitatively predicted by the original KS theory for fix-shaped vesicles.

On the other hand, at higher shear $\dot{\gamma}^* \gtrsim 1$, the shape deformation of the vesicles is not negligible. A SW phase appears between the TT and TB phases. In the SW phase, θ and α_D oscillate; see dashed lines in Figs. 3(b-

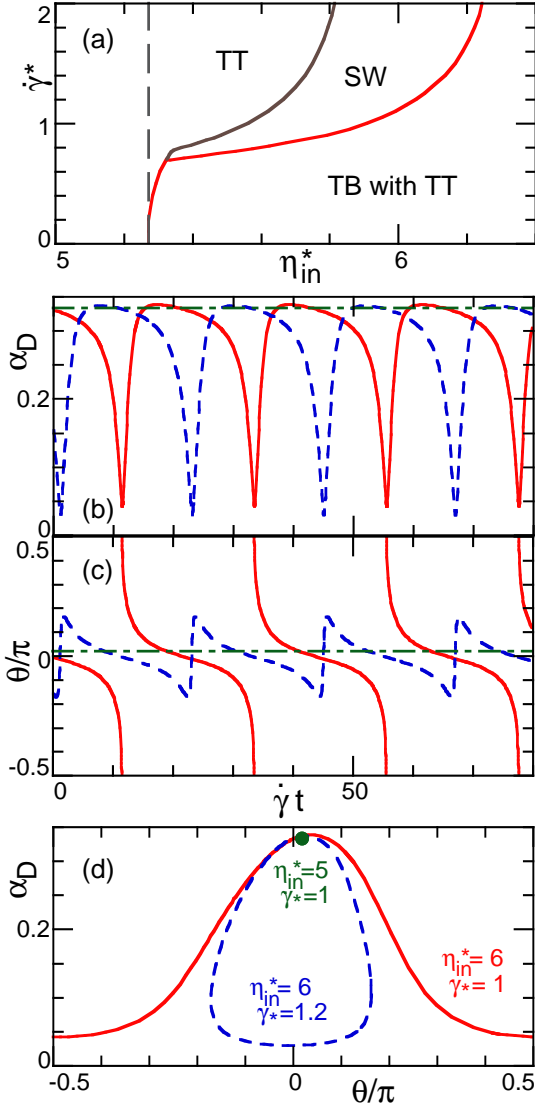


FIG. 3: (Color online) Dynamics of fluid vesicles ($k_e = 0$). (a) Phase diagram ($\eta_{in}^*, \dot{\gamma}^*$). Solid (red and brown) lines represent phase boundaries between TB, TT, and SW. For the right region of the dashed line, the vesicle passes through or remains at $\theta < 0$. (b-d) Time development of α_D and θ . Solid and dashed lines represent the TB and SW motions at $(\eta_{in}^*, \dot{\gamma}^*) = (6, 1)$ and $(6, 1.2)$, respectively. Dashed-dotted lines and closed circle represent the TT motion at $(\eta_{in}^*, \dot{\gamma}^*) = (5, 1)$.

d). These oscillations are generated by the shape deformation as follows [21]: In Eq. (1), the shear force depends on θ as $\sin(2\theta)$, so the shear increases α_D (elongation) for $0 < \theta < \pi/2$, but decreases α_D (shrinkage) for $-\pi/2 < \theta < 0$. A prolate vesicle starts θ rotation with $B < 1$ as in the TB phase and then it shrinks to a more spherical shape at $\theta < 0$, which has greater B . When B becomes greater than $1/\cos(2\theta)$, the right-hand side of Eq.(4) changes its sign and the angle θ increases. At $\theta > 0$, the vesicle elongates back to the prolate shape.

The TB-SW transition occurs when the trajectory

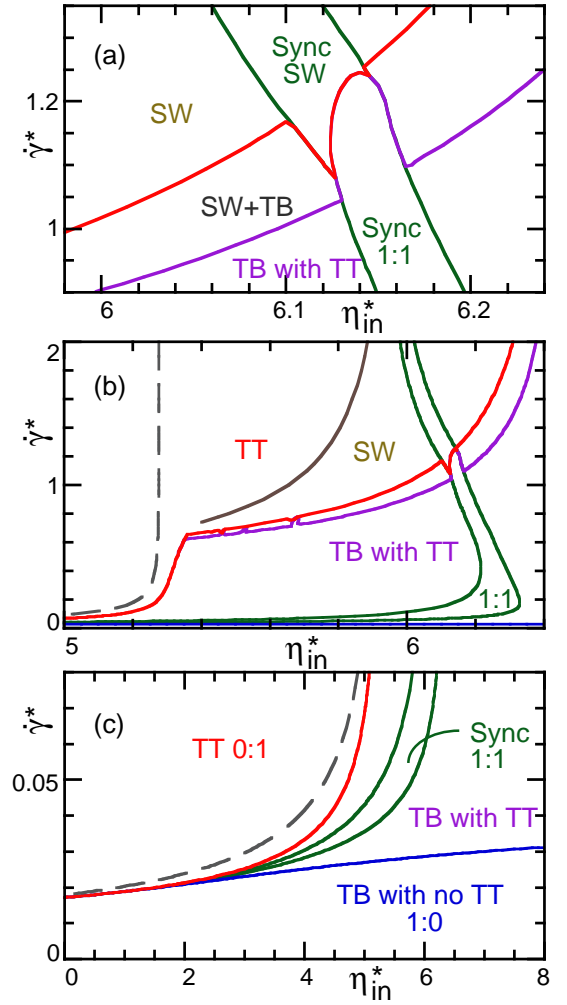


FIG. 4: (Color online) Phase diagram ($\eta_{in}^*, \dot{\gamma}^*$) of microcapsules at $k_e = 1$. (a) Enlarged figure for the region of synchronized rotation. (b) Region at high η_{in}^* . (c) Region at low $\dot{\gamma}^*$. Solid lines represent the phase boundaries. In the right region of dashed line, the vesicle passes through or remains at $\theta < 0$. Numbers represent the rotation frequencies $f_{rot}^\theta : f_{rot}^\phi$.

crosses $\alpha_D = 0$. Between $\eta_{in}^* = \eta_c^*$ (dashed line in Fig. 3(a)) and the SW phase, the TT phase has negative steady angle $\theta_0 < 0$. For fluid vesicles, the phase angle ϕ always shows rotation except for the limit $\eta_{in}^* \rightarrow \infty$. At $\eta_{in}^* \rightarrow \infty$, Eq. (4) becomes Jeffery's equation [62] for solid ellipsoidal objects, where ϕ is kept in the original position. These results show good agreement with recent experiments of lipid vesicles [7–9].

B. Microcapsule with low shear elasticity

When the membrane shear elasticity is added, the dynamics is changed from the above dynamics of fluid vesicles. First, we consider the dynamics of microcapsules at $k_e = 1$, where shear elasticity is relatively lower than the bending elasticity. The energy barrier for ϕ rotation

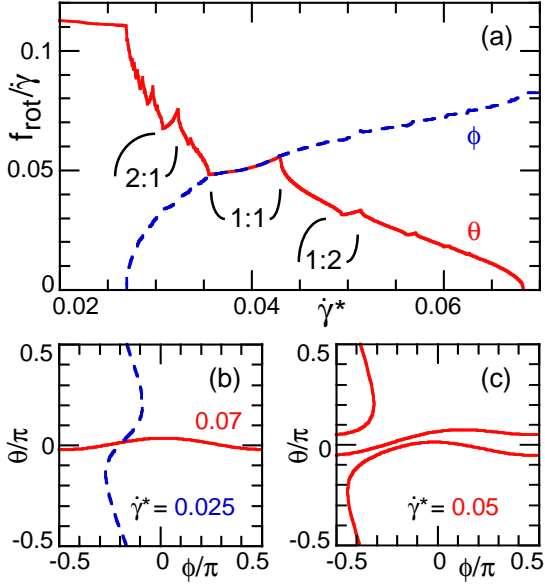


FIG. 5: (Color online) Dynamic mode transition from TB to TT phase at $k_e = 1$ and $\eta_{in}^* = 5$. (a) Rotation frequencies f_{rot} of θ (solid line) and ϕ (dashed line). (b) Trajectories of TB with $f_{rot}^\theta : f_{rot}^\phi = 1 : 0$ and TT with $f_{rot}^\theta : f_{rot}^\phi = 0 : 1$ at $\dot{\gamma}^* = 0.025$ (dashed line) and 0.07 (solid line), respectively. (c) Trajectory of TB accompanied by TT ϕ rotation with $f_{rot}^\theta : f_{rot}^\phi = 1 : 2$ at $\dot{\gamma}^* = 0.05$.

is $F^* = 0.21$ at $\phi = \pi/2$, which is five times lower than the energy barrier $F^* = 0.97$ for the capsule shrinkage at $\alpha_D = 0$. Because of this energy scale difference, the phase diagram can be separated into two regions: high shear region $\dot{\gamma}^* \gtrsim 0.8$ shown in Figs. 4(a) and (b), and low shear region $\dot{\gamma}^* \lesssim 0.1$ shown in Fig. 4(c).

1. TB-TT transition

At low shear rate $\dot{\gamma}^* \lesssim 0.1$, the shape deformation is very small so microcapsules keep their prolate shape, i.e. $\alpha_D \simeq \alpha_0$. Thus, the generalized KS theory for fix-shaped capsules proposed by Skotheim and Secomb [36] (Eq. (2) and Eq. (5) with constant α_D) predicts the phase behavior in this region very well. At very low shear rate $\dot{\gamma}^* \lesssim 0.02$, the capsules show TB motion with no TT unlike fluid vesicles; see dashed line in Fig. 5(b). The energy barrier prevents ϕ rotation. Without TT rotation, the whole capsule has to rotate (tumble) due to the shear torque applied on the capsule surface.

As $\dot{\gamma}^*$ increases, ϕ starts to rotate and then the TT frequency f_{rot}^ϕ gradually increases and the TB frequency f_{rot}^θ decreases; see Fig. 5(a). Here, an angle change of π is counted as one rotation. In this coexistence range of two rotations (TB with TT), the synchronization of ϕ and θ can occur with the integer ratios of f_{rot}^θ and f_{rot}^ϕ . This infinite number of synchronization phases is called Devil's staircase [63]. The trajectory of the synchronized

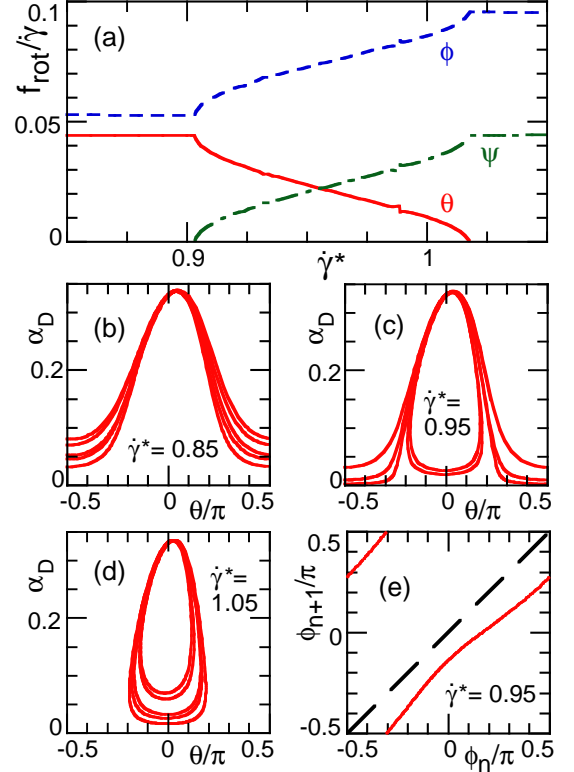


FIG. 6: (Color online) Dynamic mode transition from TB to SW phase at $k_e = 1$ and $\eta_{in}^* = 6$. (a) Rotation frequencies f_{rot} of θ (solid line), ϕ (dashed line), and swinging ψ (dashed-dotted line). (b) Trajectory at $\dot{\gamma}^* = 0.85$: TB accompanied by TT ϕ rotation. (c) Trajectory at $\dot{\gamma}^* = 0.95$: Coexistence of TB and SW motions. (d) Trajectory at $\dot{\gamma}^* = 1.05$: SW motion. (e) Return map at $\dot{\gamma}^* = 0.95$ for the angle ϕ when trajectory crosses $\theta = 0$ at $\alpha_D > 0.2$. Dashed line represents $\phi_{n+1} = \phi_n$.

rotations with $f_{rot}^\theta : f_{rot}^\phi = 1 : 2$ are shown in Fig. 5(c).

At sufficiently large $\dot{\gamma}^* > \dot{\gamma}_{tt}^*$ ($\dot{\gamma}_{tt}^* = 0.068$ at $\eta_{in}^* = 5$), θ stops rotation and the TT phase appears. With the frequency of ϕ rotation, θ and α_D oscillate (swing) around the steady values for fluid vesicles ($k_e = 0$). As $\dot{\gamma}^*$ increases, the oscillation amplitudes decrease [28, 41]. In this paper, we call this phase TT following the phase diagram of fluid vesicles (it is also called SW [28, 44, 45] or OS [46] in the previous papers). As $\dot{\gamma}^* \rightarrow \dot{\gamma}_{tt}^*$, the mean angle $\langle \theta \rangle$ approaches to null and the θ amplitude increases and then θ passes through $\theta < 0$ during this oscillation; see solid line for $\dot{\gamma}^* = 0.07$ in Fig. 5(b). This crossing region appears between the solid (red) and dashed lines in Fig. 4(c). This dashed line does not represent a phase boundary. In crossing this dashed line, the averages and amplitudes of θ and α_D show smooth change [41]. No discrete changes of trajectories are seen. This trajectory crossing $\theta < 0$ resembles the one in the SW phase of fluid vesicles. However, they are caused by a different mechanism. We call them type I and type II (swinging) oscillations. Type I: Oscillation induced by

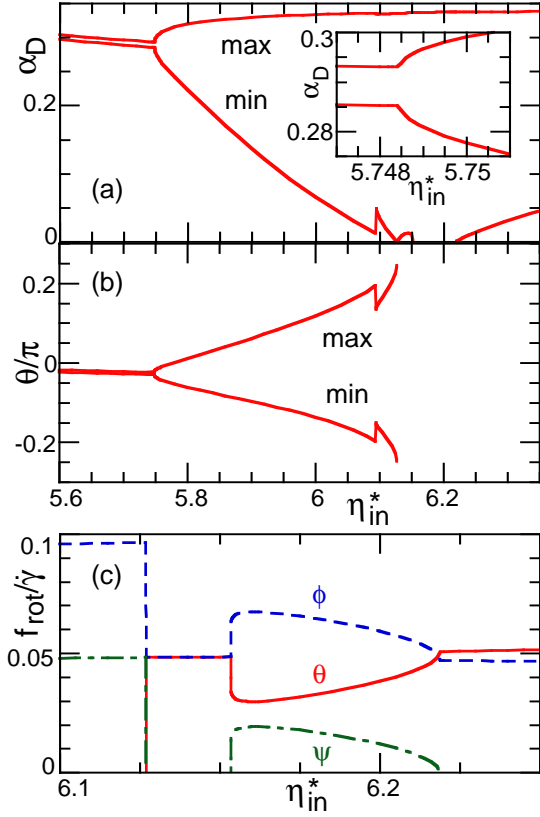


FIG. 7: (Color online) Dynamic mode transitions from TT, SW to TB phase via synchronized region at $k_e = 1$ and $\dot{\gamma}^* = 1.2$: TT for $\eta_{in}^* < 5.7484$, SW for $5.7484 < \eta_{in}^* < 6.127$, SW+TB for $6.154 < \eta_{in}^* < 6.219$, and TB with TT for $6.127 < \eta_{in}^* < 6.154$ and $\eta_{in}^* > 6.219$. Maximum and minimum of (a) α_D and (b) θ . The region around transition between TT and SW is enlarged in the inset in (a). (c) Rotation frequencies f_{rot} of θ (solid line), ϕ (dashed line), and swinging ψ (dash-dotted line).

the shape deformation. For the oscillation of fluid vesicles, the large shape deformation is essential as explained in Sec. III A. Type II: Oscillation induced by the energy barrier to ϕ rotation. This oscillation can be reproduced with a fix-shaped approximation including the passage through the negative angle θ . The resulting oscillation of the ϕ rotational velocity causes θ and α_D oscillations. These two types of oscillations cannot be distinguished only by trajectory shapes.

2. SW phase

The microcapsule at $k_e = 1$ has a SW phase around the region of the SW phase at $k_e = 0$; compare Figs. 3(a) and 4(b). In the SW phase, the type I oscillation occurs in addition to the type II oscillation. It is found that this coexistence makes the transition from TB with TT to SW a gradual change; see Fig. 6. The SW ψ frequency is calculated as a frequency of crossing $\theta = \theta_{mid}$ upwards at

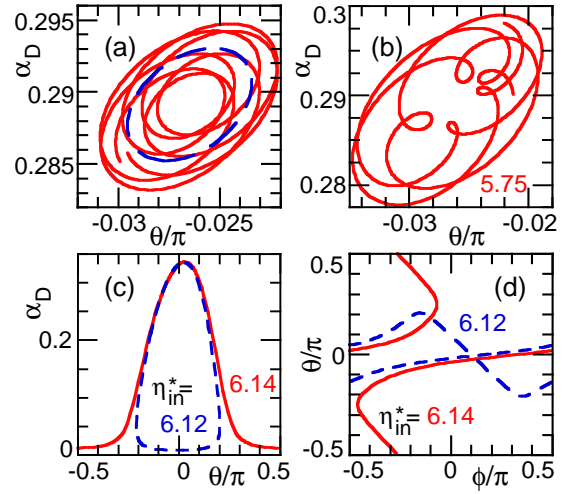


FIG. 8: (Color online) Trajectories of microcapsules at $k_e = 1$ and $\dot{\gamma}^* = 1.2$. (a) Dashed and solid lines represent trajectories in the TT phases (type II oscillation) at $\eta_{in}^* = 5.748$ and in the SW phase (unsynchronized type I and II oscillations) at $\eta_{in}^* = 5.7486$, respectively. (b) Unsynchronized oscillations with larger amplitude of the type I oscillation in the SW phase at $\eta_{in}^* = 5.75$. (c–d) Synchronized rotations in the SW phase at $\eta_{in}^* = 6.12$ (dashed line) and in the TB phase at $\eta_{in}^* = 6.14$ (solid line).

$\alpha_D < \alpha_{mid}$ in Fig. 6, where $(\theta_{mid}, \alpha_{mid})$ is a point inside the SW trajectory, and $(\theta_{mid}, \alpha_{mid}) = (0, 0.2)$ is chosen here. The type II oscillation generates the fluctuations of the TB or SW trajectories, when the oscillations and ϕ rotation are not synchronized; see return map in Fig. 6(e). As $\dot{\gamma}^*$ increases, an unsynchronized (intermittent) SW oscillation starts, and then its frequency increases while the total of the TB and SW frequencies is almost constant.

The TT-SW transition is slightly modified from fluid vesicles. Both TT and SW phases are accompanied by the type II oscillation. The transition point is detected as a discrete point of the slope of the amplitudes of α_D or θ with respect to η_{in}^* ; see the region around the transition point $\eta_{in}^* = 5.7484$ in Figs. 7(a) and (b). Two types of oscillations without synchronization are shown in Figs. 8(a) and (b).

Synchronization of type I and type II oscillations can occur with integer ratio of the oscillation frequencies. The synchronization with $f_{rot}^\theta : f_{rot}^\phi : f_{rot}^\psi = 0 : 2 : 1$ has the widest region (denoted by ‘Sync SW’ in Fig. 4(a)). Two ϕ rotations occur every θ oscillation in this region; see dashed lines in Figs. 8(c) and (d). The TB-SW transition in synchronized region ($\eta_{in}^* = 6.127$ at $\dot{\gamma}^* = 1.2$) is a discrete transition like that of the fluid vesicles; The limit cycle with $f_{rot}^\theta : f_{rot}^\phi : f_{rot}^\psi = 0 : 2 : 1$ becomes $f_{rot}^\theta : f_{rot}^\phi : f_{rot}^\psi = 1 : 1 : 0$. At the boundaries of the synchronized region ($\eta_{in}^* = 6.094$ and 6.154 at $\dot{\gamma}^* = 1.2$), the trajectories show discrete changes; see Figs. 7(a–c). Other synchronized regions with different ratios of

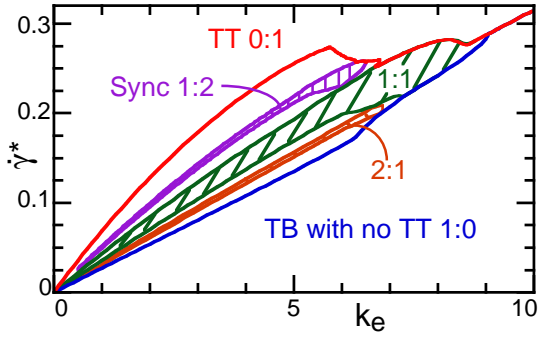


FIG. 9: (Color online) Phase diagram $(k_e, \dot{\gamma}^*)$ of microcapsules at $\eta_{in}^* = 5$. Top and bottom lines represent the phase boundaries of TT ($f_{rot}^\theta : f_{rot}^\phi = 0 : 1$) and TB with no TT ($f_{rot}^\theta : f_{rot}^\phi = 1 : 0$), respectively. Shaded regions represent synchronized phase with $f_{rot}^\theta : f_{rot}^\phi = 1 : 2, 1 : 1, \text{ and } 2 : 1$.

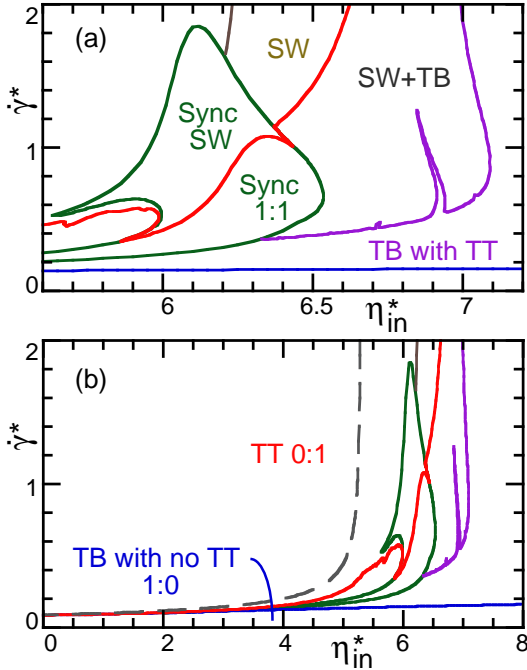


FIG. 10: (Color online) Phase diagram $(\eta_{in}^*, \dot{\gamma}^*)$ of microcapsules at $k_e = 5$. Lines represent the phase boundaries and the region with $\theta < 0$ as depicted in Fig. 4.

$f_{rot}^\theta : f_{rot}^\phi$ are seen as kinks or slits of the boundary line between 'SW+TB' and 'TB with TT' phases in Fig. 4(b).

C. Microcapsule with high shear elasticity

With increasing k_e , the phase diagram is found to show remarkable changes. Phase diagrams at $\eta_{in}^* = 5$ and at $k_e = 5, 10, \text{ and } 100$ are shown in Figs. 9–11. At $k_e \lesssim 5$, the TT-TB transition shear rates $\dot{\gamma}^*$ are approximately linear to k_e , as the height of the energy barrier for ϕ rotation linearly increases; see Fig. 9. A free-energy

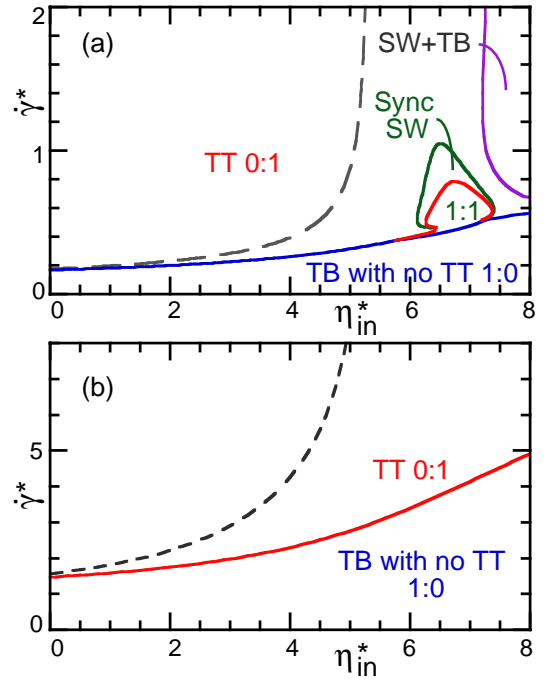


FIG. 11: (Color online) Phase diagram $(\eta_{in}^*, \dot{\gamma}^*)$ of microcapsules at (a) $k_e = 10$ and (b) $k_e = 100$. Lines represent the phase boundaries and the region with $\theta < 0$ as depicted in Fig. 4.

minimum at $\phi = \pi/2$ (or $\alpha_D < 0$ at $\phi = 0$) disappears at $k_e > k_e^c = 8.2$; see Fig. 2. Around this threshold $k_e \simeq k_e^c$, the phase behavior dramatically changes. At $k_e = 5$ (slightly below k_e^c), the TB-TT transition line becomes close to the SW phase boundary as shown in Fig. 10. The larger amplitudes of type II oscillation make the coexistence region 'SW +TB' wider. The synchronized region with $f_{rot}^\theta : f_{rot}^\phi = 1 : 1$ at the TB-SW boundary also grows from $\Delta\eta_{in}^* = 0.04$ ($k_e = 1$) to $\Delta\eta_{in}^* = 0.4$ ($k_e = 5$). A slit at $\eta_{in}^* = 6.9$ in Fig. 10 shows a synchronized region with $f_{rot}^\theta : f_{rot}^\phi = 3 : 2$. Narrower slits with different ratios of $f_{rot}^\theta : f_{rot}^\phi$ are omitted in the phase diagram in Fig. 10.

With a further increase in k_e , the region width of 'TB with TT' decreases, and then vanishes; see Figs. 9 and 11. At $\eta_{in}^* = 5$, first the regions of unsynchronized (intermittent) rotation are reduced, and the synchronized region with $f_{rot}^\theta : f_{rot}^\phi = 1 : 1$ becomes dominant. At $k_e \simeq 8$, this synchronized region only remains for 'TB with TT'. At $k_e > 9$, direct transition from 'TB with no TT' to TT phase occurs.

At $\eta_{in}^* = 100$, only two phases, TT with $f_{rot}^\theta : f_{rot}^\phi = 0 : 1$ and TB with $f_{rot}^\theta : f_{rot}^\phi = 1 : 0$, remain; see Fig. 11(b). This phase diagram agrees well with recent simulations for microcapsules with high shear elasticity at $\gamma = 100$ [44] and $\gamma \rightarrow \infty$ [46]. The rotations of ϕ and θ do not occur simultaneously at any point in the phase diagram. During tumbling, the shrinking force caused by shear elasticity prevents a passage through $\phi = \pi/2$. In

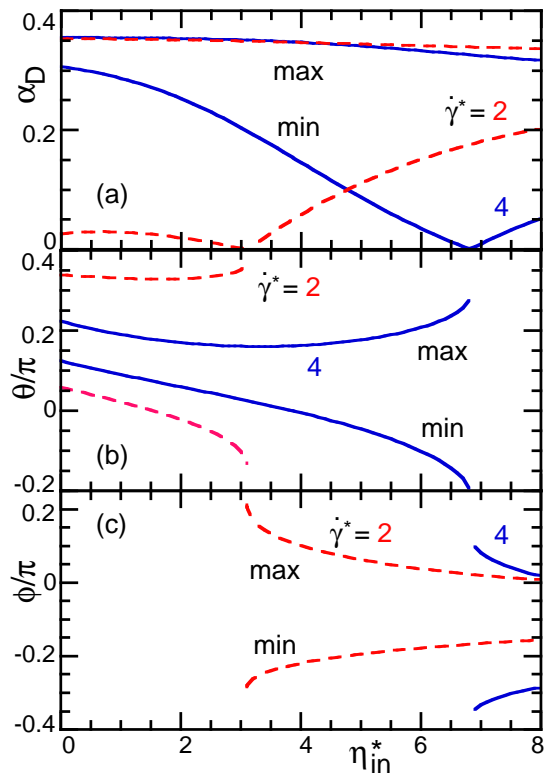


FIG. 12: (Color online) Viscosity ratio η_{in}^* dependence of maximum and minimum of (a) α_D , (b) θ , and (c) ϕ at $k_e = 100$. Dashed and solid lines represent $\dot{\gamma}^* = 2$ and 4, respectively.

the TT phase, the shear force $\propto \dot{\gamma} \sin(2\theta)$ allows the ϕ rotation through $\phi = \pi/2$. The transition between these two phases occurs when the trajectory reaches $\alpha_D = 0$ like the SW-TB transition of fluid vesicles; see Fig. 12. In the TT phase, the amplitudes of θ and α_D oscillations smoothly increase with increasing η_{in}^* ; θ and α_D oscillate with the TT frequency ($f_{rot}^\theta : f_{rot}^\phi : f_{rot}^\psi = 0 : 1 : 1$) as in the TT phase at smaller k_e . At small and large η_{in}^* , type II and type I oscillations may be dominant, respectively. However, a clear boundary of TT and SW phases is not found. The dashed line in Fig. 11(b), where the minimum of θ crosses $\theta = 0$, is not a phase boundary either.

D. Effects of a saddle point of the potential

As shown above, the phase diagram of microcapsules is changed at $k_e \simeq k_c$, where the saddle point in the free energy (the energy minimum at $\alpha_D < 0$ for $\phi = 0$ and the energy maximum in the ϕ rotation for constant α_D) vanishes. To check whether the saddle point is essential for the phase behavior or it is an accidental coincidence, the higher-order term F_3 is added to the potential. This term restores the energy minimum at $\alpha_D < 0$, while the energy profile is little modified at $\alpha_D > 0$ as shown in

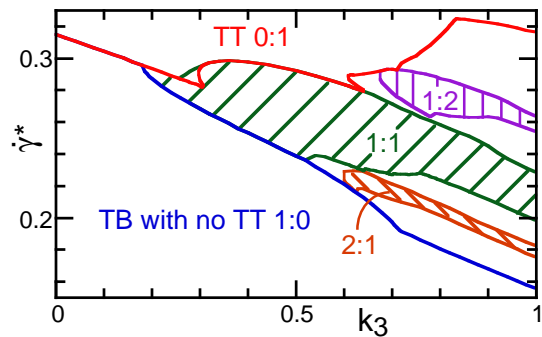


FIG. 13: (Color online) Phase diagram ($k_3, \dot{\gamma}^*$) of microcapsules at $\eta_{in}^* = 5$ and $k_e = 10$. Lines and shadowed regions represent the phase boundaries and synchronized phase, respectively, as depicted in Fig. 9. The coexistence region of two limit cycles TT ($f_{rot}^\theta : f_{rot}^\phi = 0 : 1$) and TB with TT ($f_{rot}^\theta : f_{rot}^\phi = 1 : 1$) is seen around $(k_3, \dot{\gamma}^*) = (0.3, 0.3)$.

Fig. 2. Figure 13 shows that the synchronized and intermittent regions in the phase diagram reappear with an increase in k_3 . The resulting dynamics are very similar to those at low k_e with $k_3 = 0$. Thus, the free-energy landscape for ϕ rotation is a key feature to determine the dynamics of microcapsules.

IV. DISCUSSION

Our results revealed that a saddle point of the potential changes the phase diagram of microcapsules. For prolate capsules with linear-elastic membrane at $V^* = 0.9$, the threshold of the phase diagram $k_e \sim 10$ corresponds to Föppl-von Kármán number $\gamma = Y_{mb} R_0^2 / \kappa = 1 \sim 10$, which is lower than those of typical synthetic microcapsules ($\gamma \gtrsim 100$) and RBCs ($\gamma \simeq 400$). However, the existence of a saddle point also depends on capsule shapes and buckling instability. A saddle point is observed for RBCs by experiments [64] and simulations [41] although RBCs have large γ . When an RBC is compressed in the x direction (y axis is the symmetric axis of a discocyte) with a constraint of $\phi = 0$, two dimples are buckled and new dimples appear on the x axis. These dimples generate an energy minimum at $\phi = 0$ (saddle point). Therefore, RBCs exhibit synchronized or intermittent rotations of ϕ and θ [41].

Fischer reported two types of relaxation dynamics for RBCs after the shear stops [64]. After TT motions in steady shear flow, the shear is stopped at $\phi \simeq \pi/2$. Then the RBCs return to their thermal equilibrium state by ϕ rotation or shrinkage; see Fig. 14. During the shrinkage, the buckling is observed. For microcapsules, the existence of a saddle point of the potential can be checked by the observation of this relaxation. If capsules have no saddle point, it would relax by continuous shrinkage (not by ϕ rotation). Buckling or ϕ rotation suggests an energy barrier for the shrinkage. For synthetic capsules, a sad-

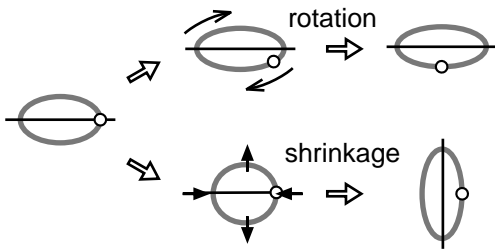


FIG. 14: Schematic representation of two relaxation pathways from $(\alpha_D, \phi) = (\alpha_0, \pi/2)$ to $(\alpha_D, \phi) = (\alpha_0, 0)$ after stopping shear flow.

dle point can be induced by buckling and nonlinear shear elasticity. At large $\gamma \gtrsim 150$, buckling transition can occur for spherical and ellipsoidal capsules [60]. Hysteresis at the buckling transition was reported in the simulation of microcapsules with $\gamma \rightarrow \infty$ for elongational flow [50]. Similar buckling may appear in shear flow.

We assumed that the major axis of the microcapsule is on the vorticity (xy) plane. This assumption is valid in most of the parameter range. Lebedev *et al.* reported spinning motion, where the major axis rotates out of the vorticity plane, at very large $\dot{\gamma}^*$ and large η_{in}^* ($\dot{\gamma}^* \gtrsim 2$ and $\eta_{in}^* \gtrsim 8$ at $V^* = 0.9$)[17]. Thus, spinning dynamics of microcapsules is also expected at large η_{in}^* but it is beyond the scope of our present study.

Here, we considered membrane with constant surface area. This condition is valid for lipid vesicles and cells, because the lipid membrane is almost incompressible. Compared to them, polymer membranes are area compressible. For microcapsules with a prolate shape, the effects of area expansion can be included by a slight modification of F and factors f_i for $0 \leq i \leq 3$ in Eqs. (1), (2), and (5). For a spherical microcapsule in the absence of flow, however, area expansion is essential, since no deformation from a sphere is allowed without area or volume change. The spherical capsules have energy minimum at $\alpha_D = 0$ so that no saddle point appear even at $\mu = 0$. Thus, the spherical capsules likely do not have ‘TB with TT’ phase.

Capsules with $V^* \lesssim 0.7$ may have multiple minima in the free-energy landscape; they would show more complicated phase behavior. Fluid vesicles with $V^* \simeq 0.6$ have three (meta-)stable states: discocyte, prolate, and stomatocyte [65]. Shear flow induces the elongating shape transition from discocyte or stomatocyte to prolate as well as the shrinking transition from prolate to discocyte [19, 20]. The transition dynamics between discocyte and prolate can be well reproduced by two differential equations of shape parameter and inclination angle θ similar to Eqs. (1) and (4). However, the transition dynamics from stomatocyte to prolate cannot be reproduced by the above two equations. At least two shape parameters are necessary to describe the direct shape change (not via discocyte) obtained in our previous simulations [20]. When shear elasticity is added to discocyte vesi-

cles, these metastable states become less stable. In our previous paper, we investigated the dynamics of RBCs at low shear rate by dynamic equations with one shape parameter [41]. At large shear rate with large η_{in}^* , RBCs can become $\alpha_D \simeq 0$, where one shape parameter may not be sufficient to describe the RBC shape.

V. SUMMARY

We have systematically studied the dynamics of prolate microcapsules in steady shear flow. The capsules exhibit four types of motions, tank-treading, tumbling, and two types of swinging oscillations. When the potential has a saddle point at the phase angle $\phi = \pi/2$ (low shear elasticity), these motions can occur simultaneously with or without synchronization. As shear rate increases at small viscosity ratio η_{in}^* , the capsules show the transition from tumbling with no tank-treading membrane rotation to tank-treading mode via coexistence of tumbling and tank-treading rotations. Swinging phase appears at large η_{in}^* and large shear rate $\dot{\gamma}^*$, where two type of swinging oscillations coexist. When the potential has no saddle point (high shear elasticity), the phase diagram is drastically changed. The coexistence phases disappear and only two phases (tank-treading and tumbling phases with no tank-treading) remain.

We have investigated only prolate capsules with a homogeneous membrane in this paper. However, our model can be applied easily to other capsules by the modification of capsule potential F . Thus, it can cover a wide range of soft objects from fluid vesicles to microcapsules and cells.

The coexistence of tumbling and tank-treading rotations has not yet been observed in experiments and simulations. Our study predicts it would occur for low shear-elastic capsules or capsules with dimples like RBCs. Further experiments and simulations are expected to confirm our predictions.

Acknowledgments

This study is supported by a Grant-in-Aid for Scientific Research on Priority Area ‘‘Soft Matter Physics’’ from the Ministry of Education, Culture, Sports, Science, and Technology of Japan.

Appendix A: Keller-Skalak Theory

In the KS theory, a vesicle is assumed to have a fixed ellipsoidal shape,

$$\left(\frac{x_1}{a_1}\right)^2 + \left(\frac{x_2}{a_2}\right)^2 + \left(\frac{x_3}{a_3}\right)^2 = 1, \quad (\text{A1})$$

where a_i denote the semi-axes of the ellipsoid, and the coordinate axes x_i point along its principal directions. The x_1 and x_2 axes, with $a_1 > a_2$, are on the vorticity (xy) plane, and the x_3 axis is in the vorticity (z) direction. The maximum lengths in three directions are $L_1 = 2a_1$, $L_2 = 2a_2$, and $L_3 = 2a_3$. The velocity field on the membrane is assumed to be

$$\mathbf{v}^m = \omega \left(-\frac{a_1}{a_2}x_2, \frac{a_2}{a_1}x_1, 0 \right). \quad (\text{A2})$$

Equations (2) and (3) of vesicle motion are derived from the energy balance between supply from the external fluid of the vesicle and dissipation inside the vesicle and on the membrane. The factors f_0 , f_1 , f_2 , and f_3 are given by

$$\begin{aligned} f_0 &= 2/(a_1/a_2 + a_2/a_1) = (1 - \alpha_D^2)/(1 + \alpha_D^2), \\ f_1 &= 0.5(a_1/a_2 - a_2/a_1) = 2\alpha_D/(1 - \alpha_D^2), \\ f_2 &= 0.5g(\alpha_1^2 + \alpha_2^2), \\ f_3 &= 0.5E_s R_0/(f_1^2 V), \\ g &= \int_0^\infty (\alpha_1^2 + s)^{-3/2} (\alpha_2^2 + s)^{-3/2} (\alpha_3^2 + s)^{-1/2} ds, \\ \alpha_i &= a_i/(a_1 a_2 a_3)^{1/3}, \end{aligned}$$

where E_s is an integral of shear stress over the membrane surface [20, 31]. At $V^* = 0.9$, we numerically obtained $f_2 = 0.3185 + 0.6\alpha_D^2 + 14\alpha_D^6 + \exp\{124(\alpha_D - 0.39)\}$.

Appendix B: Estimation of shear elastic energy

For quasi-spherical capsules, the capsule shape can be expanded in spherical harmonics $Y_{l,m}$ as $R = R_V(1 + \sum_{l,m} u_{l,m} Y_{l,m})$. Ellipsoidal shapes are described with $l = 0, 2$ modes as $R = R_V\{1 - \Delta_S/8\pi + u_{2,2}(Y_{2,2} + Y_{2,-2}) + u_{2,0}Y_{2,0}\} = R_V\{1 - \Delta_S/8\pi + \sqrt{15/8\pi}\sin^2(\theta)\cos(2\varphi)u_{2,2} + (\sqrt{5/\pi}/4)(3\cos^2(\theta) - 1)u_{2,0}\}$ with $u_{2,0}^2 + 2u_{2,2}^2 = \Delta_S/2$ in the spherical coordinate representation (R, θ, φ) . A prolate shape with $u_{2,0} = u_{2,0}^{\text{eq}} = -\sqrt{\Delta_S/2}/2$ and $u_{2,2} = u_{2,2}^{\text{eq}} = \sqrt{3\Delta_S}/4$ is chosen as a rest state in the absence of flow. The displacement is assumed in the radial direction: $\mathbf{u} = u_r \mathbf{e}_r$ with $u_r = (u_{2,2} - u_{2,2}^{\text{eq}})(Y_{2,2} + Y_{2,-2}) + (u_{2,0} - u_{2,0}^{\text{eq}})Y_{2,0}$. The shear elastic energy $\mu \int (\varepsilon_{1,1} - \varepsilon_{2,2})^2/2 + 2\varepsilon_{1,2}^2 dS$ is numerically calculated, where $\varepsilon_{i,j}$ is the two-dimensional strain tensor on the membrane surface.

-
- [1] J. M. Rallison, *Ann. Rev. Fluid Mech.* **16**, 45 (1984).
[2] H. A. Stone, *Ann. Rev. Fluid Mech.* **26**, 65 (1994).
[3] K. H. de Haas, C. Blom, D. van den Ende, M. H. G. Duits, and J. Mellema, *Phys. Rev. E* **56**, 7132 (1997).
[4] M. Abkarian and A. Viallat, *Biophys. J.* **89**, 1055 (2005).
[5] M. A. Mader, V. Vitkova, M. Abkarian, A. Viallat, and T. Podgorski, *Eur. Phys. J. E* **19**, 389 (2006).
[6] V. Kantsler and V. Steinberg, *Phys. Rev. Lett.* **95**, 258101 (2005).
[7] V. Kantsler and V. Steinberg, *Phys. Rev. Lett.* **96**, 036001 (2006).
[8] J. Deschamps, V. Kantsler, and V. Steinberg, *Phys. Rev. Lett.* **102**, 118105 (2009).
[9] J. Deschamps, V. Kantsler, E. Segre, and V. Steinberg, *Proc. Natl. Acad. Sci. USA* **106**, 11444 (2009).
[10] V. Kantsler, E. Segre, and V. Steinberg, *Phys. Rev. Lett.* **99**, 178102 (2007).
[11] M. Kraus, W. Wintz, U. Seifert, and R. Lipowsky, *Phys. Rev. Lett.* **77**, 3685 (1996).
[12] U. Seifert, *Eur. Phys. J. B* **8**, 405 (1999).
[13] C. Misbah, *Phys. Rev. Lett.* **96**, 028104 (2006).
[14] P. M. Vlahovska and R. S. Gracia, *Phys. Rev. E* **75**, 016313 (2007).
[15] G. Danker, T. Biben, T. Podgorski, C. Verdier, and C. Misbah, *Phys. Rev. E* **76**, 041905 (2007).
[16] V. V. Lebedev, K. S. Turitsyn, and S. S. Vergeles, *Phys. Rev. Lett.* **99**, 218101 (2007).
[17] V. V. Lebedev, K. S. Turitsyn, and S. S. Vergeles, *New. J. Phys.* **10**, 043044 (2008).
[18] K. S. Turitsyn and S. S. Vergeles, *Phys. Rev. Lett.* **100**, 028103 (2008).
[19] H. Noguchi and G. Gompper, *Phys. Rev. Lett.* **93**, 258102 (2004).
[20] H. Noguchi and G. Gompper, *Phys. Rev. E* **72**, 011901 (2005).
[21] H. Noguchi and G. Gompper, *Phys. Rev. Lett.* **98**, 128103 (2007).
[22] H. Noguchi, *J. Phys. Soc. Jpn.* **78**, 041007 (2009).
[23] H. Noguchi, *J. Phys. Soc. Jpn.* **79**, 024801 (2010).
[24] H. Noguchi, G. Gompper, L. Schmid, A. Wixforth, and T. Franke, *EPL* **89**, 28002 (2010).
[25] R. Skalak, *Biorheology* **27**, 277 (1990).
[26] Y. C. Fung, *Biomechanics: mechanical properties of living tissues* (Springer, Berlin, 2004), 2nd ed.
[27] T. M. Fischer, M. Stöhr-Liesen, and H. Schmid-Schönbein, *Science* **202**, 894 (1978).
[28] M. Abkarian, M. Faivre, and A. Viallat, *Phys. Rev. Lett.* **98**, 188302 (2007).
[29] M. Abkarian, M. Faivre, R. Horton, K. Smistrup, C. A. Best-Popescu, and H. A. Stone, *Biomed. Mater.* **3**, 034011 (2008).
[30] S. R. Keller and R. Skalak, *J. Fluid Mech.* **120**, 27 (1982).
[31] R. Tran-Son-Tay, S. P. Suter, and P. R. Rao, *Biophys. J.* **46**, 65 (1984).
[32] T. Nakajima, K. Kon, N. Maeda, K. Tsunekawa, and T. Shiga, *Am. J. Physiol.* **259**, H1071 (1990).
[33] N. Watanabe, H. Kataoka, T. Yasuda, and S. Takatani, *Biophys. J.* **91**, 1984 (2006).
[34] C. Pozrikidis, *Annals Biomed. Eng.* **31**, 1194 (2003).
[35] C. Pozrikidis, *Phys. Fluids* **17**, 031503 (2005).
[36] J. M. Skotheim and T. W. Secomb, *Phys. Rev. Lett.* **98**, 078301 (2007).
[37] M. M. Dupin, I. Halliday, C. M. Care, L. Alboul, and L. L. Munn, *Phys. Rev. E* **75**, 066707 (2007).
[38] R. M. MacMeccan, J. R. Clausen, G. P. Neitzel, and C. K. Aidun, *J. Fluid. Mech.* **618**, 13 (2009).

- [39] H. Noguchi and G. Gompper, Proc. Natl. Acad. Sci. USA **102**, 14159 (2005).
- [40] J. L. McWhirter, H. Noguchi, and G. Gompper, Proc. Natl. Acad. Sci. USA **106**, 6039 (2009).
- [41] H. Noguchi, Phys. Rev. E **80**, 021902 (2009).
- [42] K. S. Chang and W. L. Olbricht, J. Fluid Mech. **250**, 609 (1993).
- [43] A. Walter, H. Rehage, and H. Leonhard, Colloids Surf. A **183-185**, 123 (2001).
- [44] S. Kessler, R. Finken, and U. Seifert, J. Fluid Mech. **605**, 207 (2008).
- [45] Y. Sui, H. T. Low, Y. T. Chew, and P. Roy, Phys. Rev. E **77**, 016310 (2008).
- [46] P. Bagchi and R. M. Kalluri, Phys. Rev. E **80**, 016307 (2009).
- [47] S. Kessler, R. Finken, and U. Seifert, Eur. Phys. J. E (2009).
- [48] E. Lac and D. Barthès-Biesel, Phys. Fluids **20**, 040801 (2008).
- [49] Y. Lefebvre, E. Leclerc, D. Barthès-Biesel, J. Walter, and F. Edwards-Lévy, Phys. Fluids **20**, 123102 (2008).
- [50] W. R. Dodson III and P. Dimitrakopoulos, Phys. Rev. Lett. **101**, 208102 (2008).
- [51] K. Tsubota and S. Wada, Phys. Rev. E **81**, 011910 (2010).
- [52] N. Elsner, F. Dubreuil, and A. Fery, Phys. Rev. E **69**, 031802 (2004).
- [53] H. Sakai, K. Tanaka, H. Fukushima, K. Tsuchiya, K. Sakai, T. Kondo, and M. Abe, Colloids Surf. B Biointerfaces **66**, 287 (2008).
- [54] H. N. Yow, X. Wu, A. F. Routh, and R. H. Guy, Eur. J. Pham. Biopham. **72**, 62 (2009).
- [55] L. D. Landau and E. M. Lifshitz, *Theory of elasticity* (Pergamon Press, Oxford, 1986), 3rd ed.
- [56] N. Mohandas and E. Evans, Annu. Rev. Biophys. Biomol. Struct. **23**, 787 (1994).
- [57] G. Lenormand, S. Hénon, A. Richert, J. Siméon, and F. Gallet, Biophys. J. **81**, 43 (2001).
- [58] J. P. Mills, L. Qie, M. Dao, C. T. Lim, and S. Suresh, Mech. Chem. Biosys. **1**, 169 (2004).
- [59] M. Dao, J. Li, and S. Suresh, Mater. Sci. Eng. C **26**, 1232 (2006).
- [60] J. Lidmar, L. Mirny, and D. R. Nelson, Phys. Rev. E **68**, 051910 (2003).
- [61] H. L. Goldsmith and J. Marlow, Proc. R. Soc. Lond. B **182**, 351 (1972).
- [62] G. B. Jeffery, Proc. R. Soc. London Ser. A **102**, 161 (1922).
- [63] P. Bergé, Y. Pomeau, and C. Vidal, *Order within chaos: towards a deterministic approach to turbulence* (Wiley, New York, 1984).
- [64] T. M. Fischer, Biophys. J. **86**, 3304 (2004).
- [65] U. Seifert, Adv. Phys. **46**, 13 (1997).